



Accelerated Design of Architected Materials with Multifidelity Bayesian Optimization

Chengyang Mo, Ph.D.¹; Paris Perdikaris, Ph.D.²; and Jordan R. Raney, Ph.D.³

Abstract: In this work, we present a multifidelity Bayesian optimization framework for designing architected materials with optimal energy absorption during compression. Data from both physical experiments (high fidelity) and numerical simulations (low fidelity) are fed in parallel to train the surrogate model, which iteratively decides the next sets of experiments and simulations to run in order to find the optimal structural parameters. We show that having multifidelity data sources allows the optimization framework to find the optimum after fewer iterations relative to using a single high-fidelity source. This saves both material costs and time in the optimization process. Finally, we also apply constraints (on relative density and stress variations) to the optimization process, finding optimal structures within the bounds of the constraints. This framework can be translated to other problems that require complex, high-fidelity, labor-intensive experiments while automating low-fidelity simulations. **DOI:** 10.1061/JENMDT.EMENG-7033. © 2023 American Society of Civil Engineers.

Introduction

Advanced manufacturing has enabled the design and fabrication of architected materials with ever-increasing structural complexity, enabling research aimed at understanding new structures with high specific stiffness/strength (Zheng et al. 2014; Meza et al. 2014; Jiang and Pikul 2021), energy absorption (Portela et al. 2021; Yin et al. 2019), or fracture resistance (Mirkhalaf et al. 2014; Pham et al. 2019; Torres et al. 2019). For layer-by-layer manufacturing methods, it is often pointed out that complexity comes for free. Yet, most work on architected materials has remained focused on periodic and uniform structures (Zheng et al. 2014). This is partly due to the large number of design parameters that are introduced when periodicity is no longer required. There is a lack of systematic methods for designing such structures. Instead, the design process for architected solids with nonuniformity has mostly relied upon intuition, leading to simple design motifs such as density gradients (Montgomery et al. 2021; Chen et al. 2022), or motifs inspired by nature [e.g., bamboo (Dixon and Gibson 2014)] or metallurgy [e.g., polycrystalline metals inspired by grain boundaries and precipitates (Pham et al. 2019; Liu et al. 2021)].

To build structures that take advantage of the design freedom afforded by advanced manufacturing, a systematic and algorithmic design method is needed. With the improved computing power and design algorithms available in recent years, machine learning (ML) and artificial intelligence (AI) have been increasingly used to identify relationships between parameter space and property space. Deep learning has been used to design multiphase composites with

Note. This manuscript was submitted on October 28, 2022; approved on December 12, 2022; published online on March 30, 2023. Discussion period open until August 30, 2023; separate discussions must be submitted for individual papers. This paper is part of the *Journal of Engineering Mechanics*, © ASCE, ISSN 0733-9399.

improved fracture resistance (Gu et al. 2018; Yang et al. 2020; Yu et al. 2019), graphene kirigami with improved ductility (Hanakata et al. 2018), and composite designs with elastic properties approaching the Hashin-Strikman bound (Mao et al. 2020).

However, for deep learning methods, the quality of the optimization is highly dependent on the quality of the data provided to train the algorithm. Moreover, due to the large amount of data required, it is often not practical to use deep learning methods with experimental data, which is typically laborious or expensive to obtain. Topology optimization is another technique that has been implemented for problems of large size in compliance (Santer and Pellegrino 2009), stiffness (Buhl et al. 2000; Da et al. 2022), and fracture of lattice structures (Da and Qian 2020; Song et al. 2019). Typically, topology optimization is performed using numerical simulations that can be difficult to translate to experiments.

Unlike deep learning methods, active learning or autonomous experimentation (AE) allow iterative evaluation of properties guided by machine learning algorithms, a process that can be automated (Stach et al. 2021). A surrogate model is trained using existing data to identify trends and to learn the representation of the entire space. For a given iteration, a planning algorithm chooses what experiment to conduct next by minimizing a certain function based on its current understanding of the entire space. Lastly, the existing data are updated with the new evaluation. This iterative loop continues until an objective is achieved.

One of the most commonly used active learning frameworks is Bayesian optimization (BO), which is built upon Bayesian statistics, using a Gaussian process as the surrogate model providing prediction for the entire space (Snoek et al. 2012). BO has proved to be successful in a variety of contexts, including chemistry (Santos et al. 2019; Zhong et al. 2020; Burger et al. 2020), material discovery (Li et al. 2020; Yuan et al. 2018; Xue et al. 2016; Meredig et al. 2018; Balachandran et al. 2018), design of inks for three-dimensional (3D) printing (Erps et al. 2021), and, most recently, design of architected materials (Gongora et al. 2020; Vangelatos et al. 2021). Aside from engineering applications, BO is also widely used as a tool for hyperparameter tuning for other machine learning models. BO has numerous advantages compared with other AE methods (Frazier 2018): (1) only a small number of initial data points are required (one is sufficient); (2) uncertainty is inherently built into the Gaussian process (GP); and (3) it offers relative ease of implementation for a variety of problems.

¹Dept. of Mechanical Engineering and Applied Mechanics, Univ. of Pennsylvania, Philadelphia, PA 19104. ORCID: https://orcid.org/0000-0002-8960-2467. Email: chengymo@seas.upenn.edu

²Professor, Dept. of Mechanical Engineering and Applied Mechanics, Univ. of Pennsylvania, Philadelphia, PA 19104. Email: pgp@seas.upenn.edu

³Professor, Dept. of Mechanical Engineering and Applied Mechanics, Univ. of Pennsylvania, Philadelphia, PA 19104 (corresponding author). ORCID: https://orcid.org/0000-0001-5329-9980. Email: raney@seas.upenn.edu

Previous endeavors have proven the efficiency of using BO to explore the design space of architected materials with complex geometry. It has been shown that this can be much faster than conventional approaches (Gongora et al. 2020; Vangelatos et al. 2021). However, these previous works only made use of either numerical simulations exclusively or experiments exclusively to perform the optimization process. Optimization solely via experimental data is typically very laborious or requires specialty robotic systems. On the other hand, optimization solely via numerical simulations inherently assumes that the simulations accurately capture the full complexity of experiments, something that is rarely accomplished without significant expertise and computational resources. Hence, the optimum obtained from BO that relies only on numerical simulations does not guarantee that the true experimental optimum has been reached. One recent effort to incorporate both experiments and simulations has shown promise as a follow up to previous BO efforts in architected materials, although it is limited to a discrepancy model with elastic properties (Gongora et al. 2021).

In this work, we propose a multifidelity Bayesian optimization (MFBO) framework for designing architected materials with optimal failure properties via nonuniform distribution of strut thickness. Multifidelity Bayesian optimization has been used to optimize properties through numerical simulation with different computational costs (Solomou et al. 2018; Couperthwaite et al. 2020; Chen et al. 2021). Here, we will use multifidelity data that incorporate low-fidelity numerical simulations and high-fidelity experiments in parallel, both providing predictions for the same property.

Problem Setup

In this work, we aim to optimize the compressive failure properties of nonuniform 2D cellular structures, as illustrated in Fig. 1(a). Applying a mirror symmetry as shown in Fig. 1(a) results in a lattice with 16 parameters. Each of these corresponds to the width of the three half struts belonging to a particular triangle (with the centerlines of the original uniform lattice defining the boundaries between half widths in adjacent triangles). These parameters are bounded from 0.5 to 1 mm. This selection of parameters and parameters bounds maintains a number of variables that is currently feasible for optimization with BO (Frazier 2018).

The properties of interest are the energy absorption E_{ab} , plateau stress variation $\text{var}(\sigma_{\text{pl}})$, and the relative density. The energy absorption E_{ab} is calculated as the area under the stress–strain curve that is bounded by the densification slope, linearly interpolated with the densification portion of the stress–strain curve (Gibson and Ashby 1997) [shaded area in Fig. 1(b)]. By extrapolating the densification slope, we identify the densification strain ε_d (Gibson and Ashby 1997). The variation of plateau stress is the variance of the stress along the plateau of the stress–strain curve [Fig. 1(b)], i.e., for the plateau region $(\varepsilon_y < \varepsilon < \varepsilon_d)$ we calculate

$$var(\sigma_{pl}) = SD(\sigma_{pl})/\sigma_{pl}^* \tag{1}$$

where σ_{pl}^* = average value of plateau stress σ_{pl} . The variance of plateau stress quantifies how flat the plateau stress is (fully flat being zero). This property is important because it quantifies the stability of

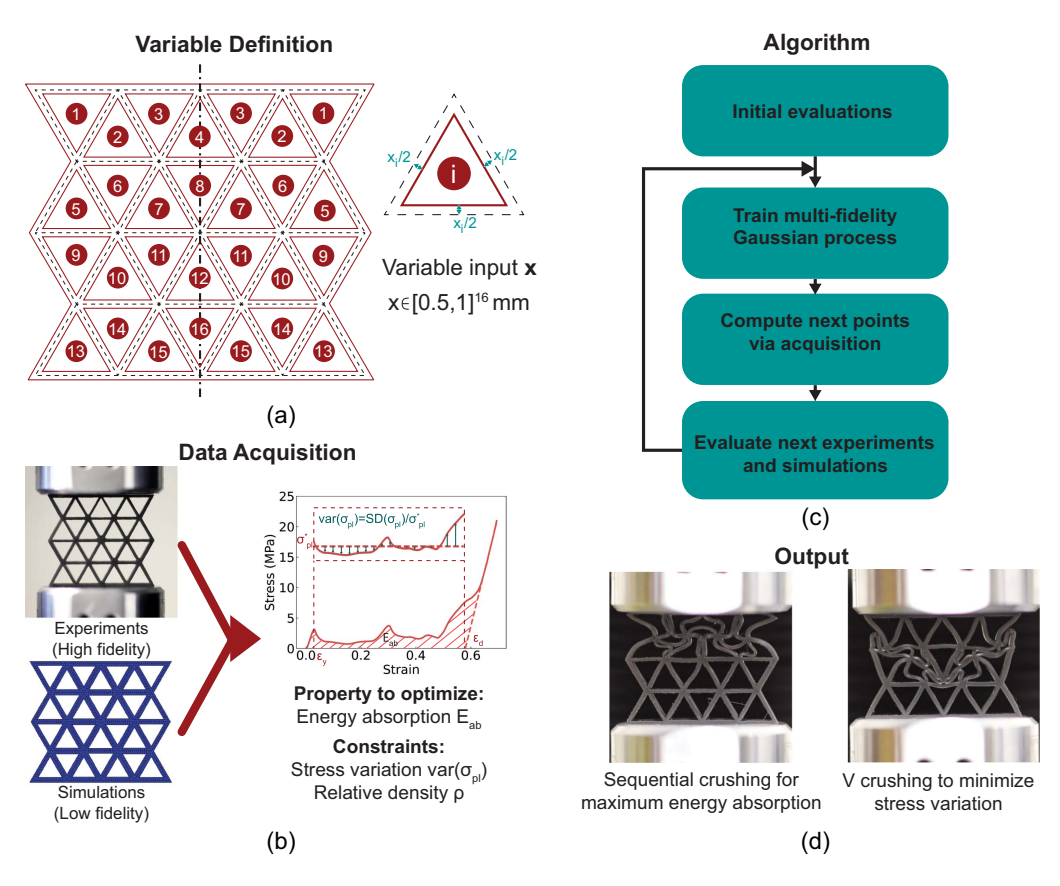


Fig. 1. (a) Input consisting of 16 parameters, each representing the half strut width corresponding to one of the numbered triangles; (b) experiments and simulations are conducted to measure the stress–strain properties of the structures when subjected to in-plane compression, and mechanical properties of interest are extracted from this data; (c) flowchart of the Bayesian optimization algorithm, including (1) training of the Gaussian process; (2) the next set of parameters are selected by the acquisition function; and (3) evaluation via experiment or simulation, according to loop; and (d) optimized architectures reveal two different patterns of deformation: layer-by-layer crushing is observed when the optimization algorithm targets maximal energy absorption; however, if the constraint to minimize stress variation is enforced, a V-shape deformation pattern is observed.

the structure during compression. Low values of plateau stress variance are desirable for protective materials because they are less likely to allow spikes in stress that cause damage. These properties are quantified using both high-fidelity experiments and low-fidelity simulations. Both methods provide the full stress–strain curve during compression up to densification, from which the properties of interest are extracted. Lastly, we are also interested in the relative density of the lattice structures (i.e., the total mass of the lattice structure divided by the mass of solid material of the same volume), which can be computed from the input parameters.

The workflow is shown in Fig. 1(c) and is as follows:

- Train the multifidelity Gaussian process, which incorporates two types of data: high-fidelity experiments and low-fidelity numerical simulations.
- 2. Use the trained Gaussian process model. The next point of evaluation is determined by minimizing the acquisition function with a numerical minimizer with random starting points in the entire space. In addition to random start points, the evaluated variables of low-fidelity sources are also used as starting points of the minimization, maximizing the use of low-fidelity data sources.
- Perform the next experiment or simulation, feeding the result of this evaluation back to the Gaussian process model for the next iteration.

After a number of iterations of data acquisition and surrogate model updates, we observed evidence of convergence via close clustering of predicted optimal geometries. Our workflow allows parallel integration of both data streams, which are fed into the surrogate model simultaneously. Examples of geometries that reach optimized properties are illustrated in Fig. 1(d). (Layer-by-layer crushing is observed when the objective is maximum energy absorption; a V-shaped buckling pattern is more common when the objective is to minimize plateau stress variation.)

In-Plane Compressive Behavior of Nonuniform Triangular Lattices

Throughout the study, we have conducted over 3,000 numerical simulations and 120 experiments in which we extracted the stress-strain behavior of the nonuniform triangular lattice during compression. Fig. 2 shows the corresponding results of all simulations and experiments. We plot the energy absorption versus the variance of plateau stress and versus the relative density in Figs. 2(a and b), respectively, for all simulations. We observed positive linear correlation between the energy absorption and relative density, although it is less strong with variance of plateau stress. However, the best-performing structure in terms of energy absorption was not the structure with the highest relative density (i.e., a uniform lattice with all strut widths maximized).

The experimental stress–strain plots are shown in Fig. 2(c). The yield, plateau stress, and densification strain varied significantly among the experiments. For each lattice that was tested experimentally, we also conducted a numerical simulation. One of the key prerequisites for MFBO to work well is that there is a strong correlation between high- and low-fidelity data. Specifically, we assumed a linear relationship in the formulation of MFBO. Fig. 2(d) plots the energy absorption measured experimentally for each test (high-fidelity) versus the energy absorption for the corresponding lattice measured via simulation (low-fidelity), confirming the linear correlation.

Results

Prior works have quantified the advantage of single-fidelity Bayesian optimization compared with conventional experimental design (Gongora et al. 2020) and alternative optimization algorithms (Vangelatos et al. 2021). As shown in Fig. S1, BO was more efficient than gradient descent at optimizing for energy absorption

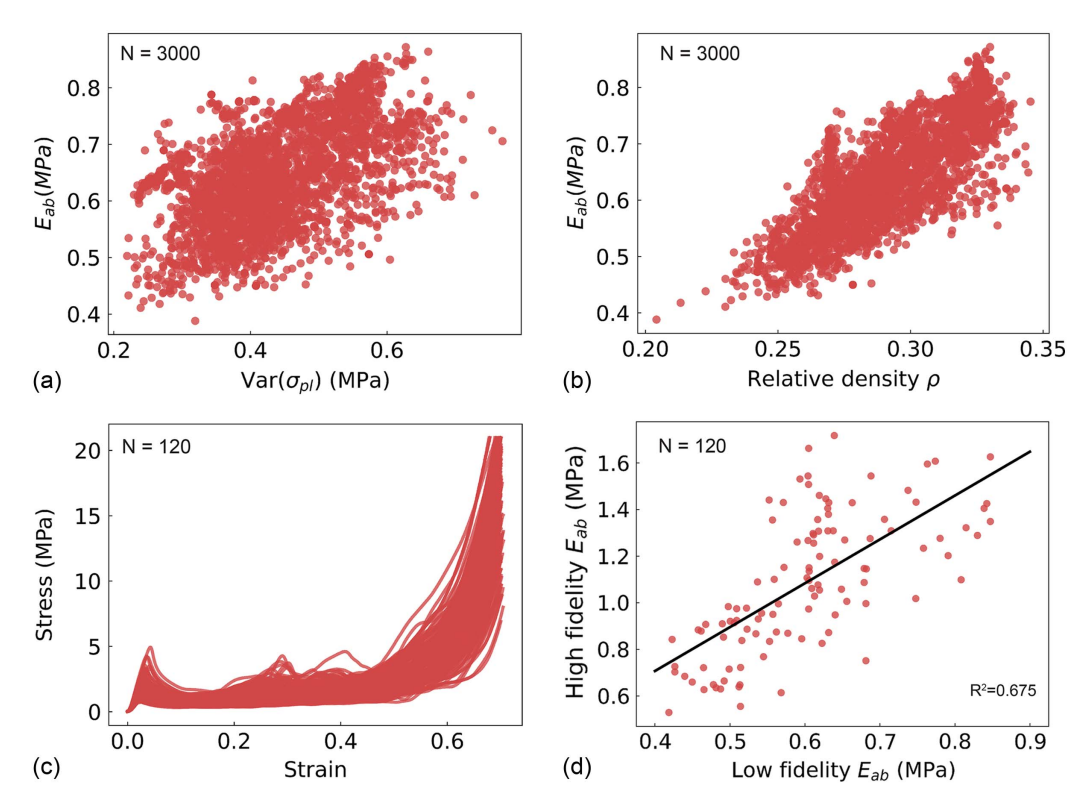


Fig. 2. (a) Energy absorption versus variation of plateau stress for all numerical simulations; (b) energy absorption versus relative density for all numerical simulations; (c) all stress–strain curves of the experiments; and (d) energy absorption extracted from experiments (high-fidelity) versus simulations (low-fidelity).

of the lattice during compression. This is largely due to the fact that the properties of interest in this work have a nonlinear dependence on the parameters (making gradient computations less efficient). The cost of running the optimization solely via high-fidelity experiments (no low-fidelity numerical simulations) would be extremely high (more than 100 experiments). This shows that the design process is greatly accelerated through the application of MFBO to the lattice optimization problem.

We ran two parallel schemes to evaluate the benefit of using multiple data sources in BO. The first used only high-fidelity experiments as the data input in BO; the second used both high-fidelity experiments and low-fidelity simulations as parallel multifidelity data for BO. Fig. 3(a) shows the energy absorption of tested structures versus the number of iterations of experiments. We also plot the accumulated maximum properties [dashed lines in Fig. 3(a)], showing the evolution of optimization. Prior to performing multifidelity BO, a low-fidelity-only BO was allowed to run for 150 iterations to generate the starting set of parameters for the multifidelity BO.

First, we observed that after just a few iterations of MFBO, a lattice with better energy absorption was found compared with the initial lattice, which is the best candidate provided by low-fidelity BO. Moreover, multifidelity BO was able to find structures with energy absorption up to 35% higher than the best-performing structures in high-fidelity only BO (actual numbers are summarized in Table 1). On top of that, 5 out of 20 experiments exhibited better energy absorption from the multifidelity campaign. Hence, not only did multifidelity BO find a better optimum (35% improvement), it also produced several candidates with higher energy absorption than high-fidelity BO.

To track the convergence status of the algorithm, we probed the surrogate model (Gaussian process) of each campaign at the end of 20 high-fidelity experiments. This was done by restarting the training of the Gaussian process a total of 50 times with the same inputs. For each restart, the 50 best candidates were predicted by the surrogate model using the same acquisition function. We characterized the state of the predicted candidates using intercluster distance.

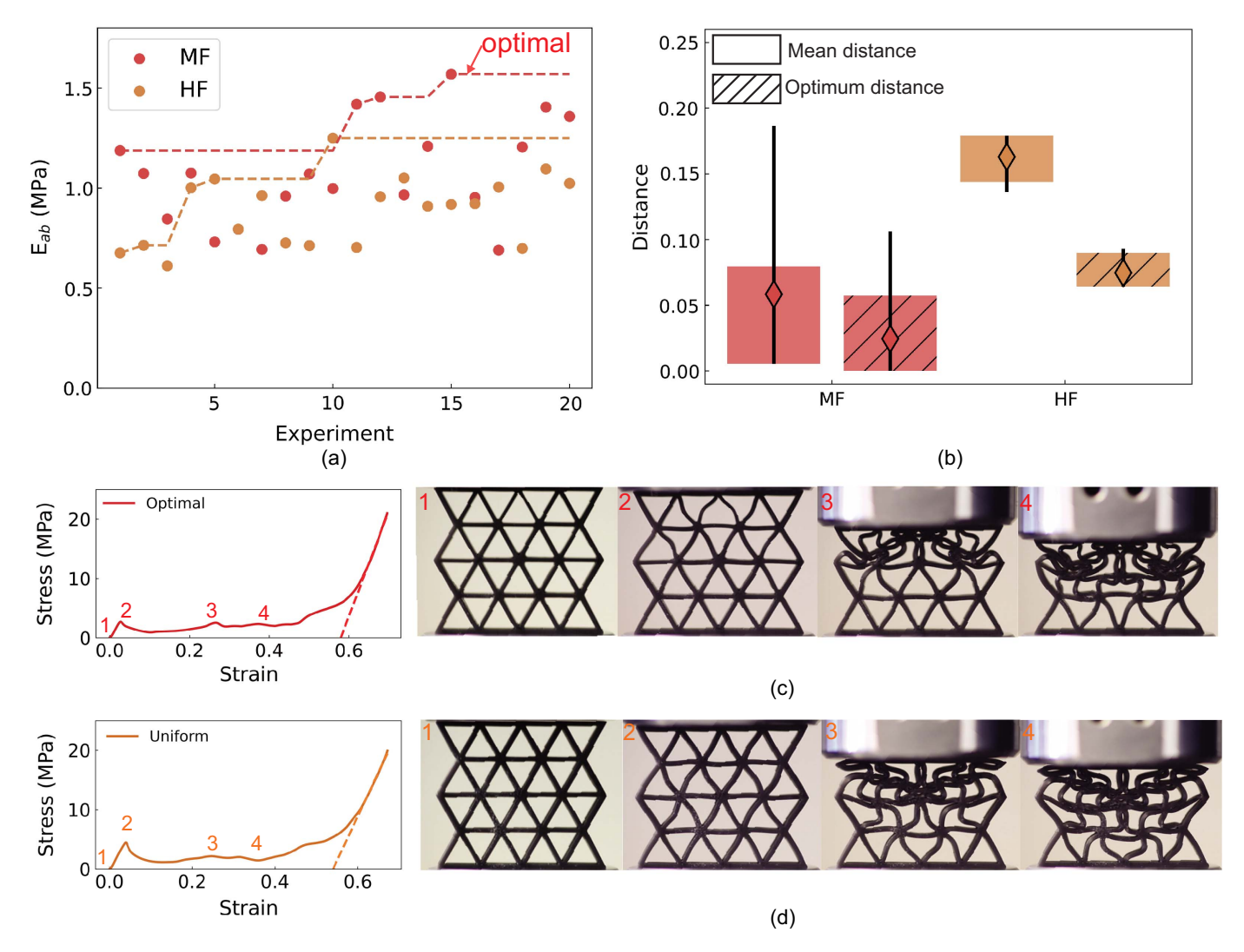


Fig. 3. Optimization for maximal energy absorption: (a) evolution of experimental evaluations for both multifidelity and high-fidelity-only campaigns; (b) state of the surrogate model after 20 iterations of experiments for multifidelity and high-fidelity-only campaigns, based on 50 structures predicted to be optimal by the model; two cluster distances are computed for each campaign, one relative to the mean of the predicted optimal structures, and one relative to the structure with the most optimal performance; (c) measured stress—strain behavior and optical images of the deformed lattice at various stages of compression (Video S1); data correspond to the best-performing lattice (maximal energy absorption); and (d) stress—strain behavior and optical images of the deformed lattice at various stages of compression (Video S2); data correspond to a uniform lattice with the struts of maximum allowed width.

Table 1. Summary of properties for the best-performing lattice from each BO iteration conducted in this study

Lattice type	$ ho_c$	E_{ab} (MPa)	$\mathrm{Var}(\sigma_{pl})$	Total number of experiments	
Uniform lattice	0.3464	1.369	0.4790	N/A	N/A
High-fidelity BO	0.2995	1.2487	0.5637	20	0
Multifidelity BO	0.3228	1.5685	0.5186	20	200
VF constrained	0.2782	1.4610	0.7139	20	200
$\underline{\mathrm{Var}(\sigma_{pl})}$ constrained	0.2996	1.5417	0.4925	40	400

This quantifies how close the candidates are to each other (mean distance) and to the optimal geometry (optimum distance). The intercluster distance was calculated as follows:

$$S = \left[\frac{1}{N} \Sigma \|x_i - x^*\|^2 \right]^{1/2} \tag{2}$$

where x_i = new candidates. For the mean distance, x^* is the mean of all new candidates. For the optimal distance, x^* is the location of the maximum energy absorption, as shown in Fig. 3(a).

Fig. 3(b) shows the mean distance and the optimal distance for both multifidelity and high-fidelity-only BO. The bars indicate the 95% confidence bound for all 50 restarts. The diamonds and lines represent the mean and range, respectively. For multifidelity BO, the distance between new candidates was very small. This indicates that the BO process has converged, yielding predictions of optimal parameter sets within a narrow region. On the other hand, the predictions from BO with only high-fidelity had a mean distance almost three times larger than that of the multifidelity BO. The predictions from multifidelity BO were also much closer to the optimal geometry obtained in the experiments. This shows that even by only running 20 experiments, multifidelity BO can reach convergence and lead to better properties.

Fig. 3(c) shows the stress–strain behavior of an optimal lattice, as well as images of the deformed lattice at different applied strains. At Position 2, corresponding to the yield point, the triangle with the thinnest struts buckles first. This causes a postyield drop in stress. Subsequently (Position 3), the top two layers of the structure undergo densification. Additional peaks in the result from sequential buckling of the next two layers (i.e., Layers 3 and 4). The optimal geometry was similar to a uniform lattice with struts of maximum-allowed thickness.

The stress–strain behavior and images of the deformation are shown in Fig. 3(d) for this uniform lattice. Unlike the optimal structure, the uniform lattice had a yield stress of 4 MPa, whereas the optimal structure yielded at 2.5 MPa. This result was expected because all struts are uniform with maximum thickness. However, because a larger number of struts yielded at the same times [Position 2 in Fig. 3(d)], there is a steeper postyield drop, leading to a plateau stress of 0.9 MPa during subsequent loading (Positions 3 and 4) compared with 1.2 MPa for the plateau stress of the optimal structure. As a result, despite having a significantly higher yield stress, the uniform lattice absorbs only 95% the energy of the optimal lattice.

Moreover, the large stress variations of the uniform lattice make it less suitable in many applications, where uniform stresses are paramount in order to protect adjacent objects. Some degree of stochasticity can increase the energy absoprtion, as has been shown for natural materials, although often at the cost of reduced strength [e.g., bamboo (Habibi and Lu 2014) and honeycomb (Smith et al. 2021)].

Optimization for Total Energy Absorption with Constraints

Bayesian optimization is also compatible with the implementation of constraints. Here, we present two example problems for constrained optimization: one with a deterministic constraint, namely, the relative density, as determined from input parameter \mathbf{x} ; the other constraint is related to separate properties, namely, the variation in plateau stress, which is estimated via an independent Gaussian process. The constraints are enforced via the acquisition function as follows ("Materials and Methods" section):

$$\min_{\mathbf{x}} LCB(\mathbf{x}) P(y_c(\mathbf{x}) \le 0) \tag{3}$$

where $c(\mathbf{x})$ = constraint function. The probability that the lattice satisfies a constraint on relative density is deterministic, as represented by a Heaviside function

$$P(y_c(\mathbf{x}) \le 0) = \rho(\mathbf{x}) \le \rho_c \tag{4}$$

For constraints on the variation of plateau stress, we introduce an independent Gaussian process that estimates the constraint. The probability of constraint satisfaction can be estimated from the output of the Gaussian process as follows:

$$P(y_c(\mathbf{x}) \le 0) = \frac{1}{2} \left[1 - \operatorname{erf}\left(\frac{\mu_c(\mathbf{x})}{\sigma_c(\mathbf{x})\sqrt{2}}\right) \right]$$
 (5)

where $\mu_c(\mathbf{x})$ and $\sigma_c(\mathbf{x})$ = outputs from the Gaussian process for constraint estimation \mathcal{GP}_c .

Because the constraint is enforced within the acquisition function, it does not generate discontinuity in the property space, leading to better performance of the Gaussian process for estimating the property that we are optimizing. We first conducted campaigns using only low-fidelity simulations for constraining the relative density below 0.28. As shown in Fig. S2, by applying a constraint on relative density, our BO algorithm was able to only probe structures that satisfy the relative density constraint. In fact, the majority of evaluations had the maximum relative density allowed, leading to optimal structures that satisfy the constraint in under 100 iterations.

Multifidelity BO exhibited similar results, as shown in Figs. 4(a and b). Through 20 iterations, all experimental evaluations were performed with geometries that satisfy the constraint, as illustrated by the dashed line in Fig. 4(b). Numerous evaluations were conducted with a relative density of 0.28. The structure with maximum energy absorption was not found on the constraint line. The best-performing geometry and its corresponding stress—strain curve is shown in Fig. 4(c) (with actual measured properties given in Table 1). The deformation pattern of the lattice during compression is similar to the optimal lattice shown in Fig. 3(c), where each layer is sequentially crushed.

Next, we optimized energy absorption of the lattice while limiting the variance of plateau stress. This constraint was more difficult to satisfy than a constraint on relative density because it was estimated by an independent Gaussian process. We first conducted campaigns with only low-fidelity simulations. As shown in Fig. S3, not all evaluations satisfied the constraint. Hence, it required more iterations to reach convergence. A portion of iterations was used to learn the constraint space, in addition to the iterations used to learn the property space.

We also conducted a multifidelity campaign with a constraint on the variance of the plateau stress. We conducted 40 experiments, leading to improvement of energy absorption without the variance of plateau stress exceeding 0.5. Fig. 5(a) shows the property evaluation for each experiment. Whether or not the constraint was satisfied is indicated. Fig. 5(b) plot the energy absorption versus variance

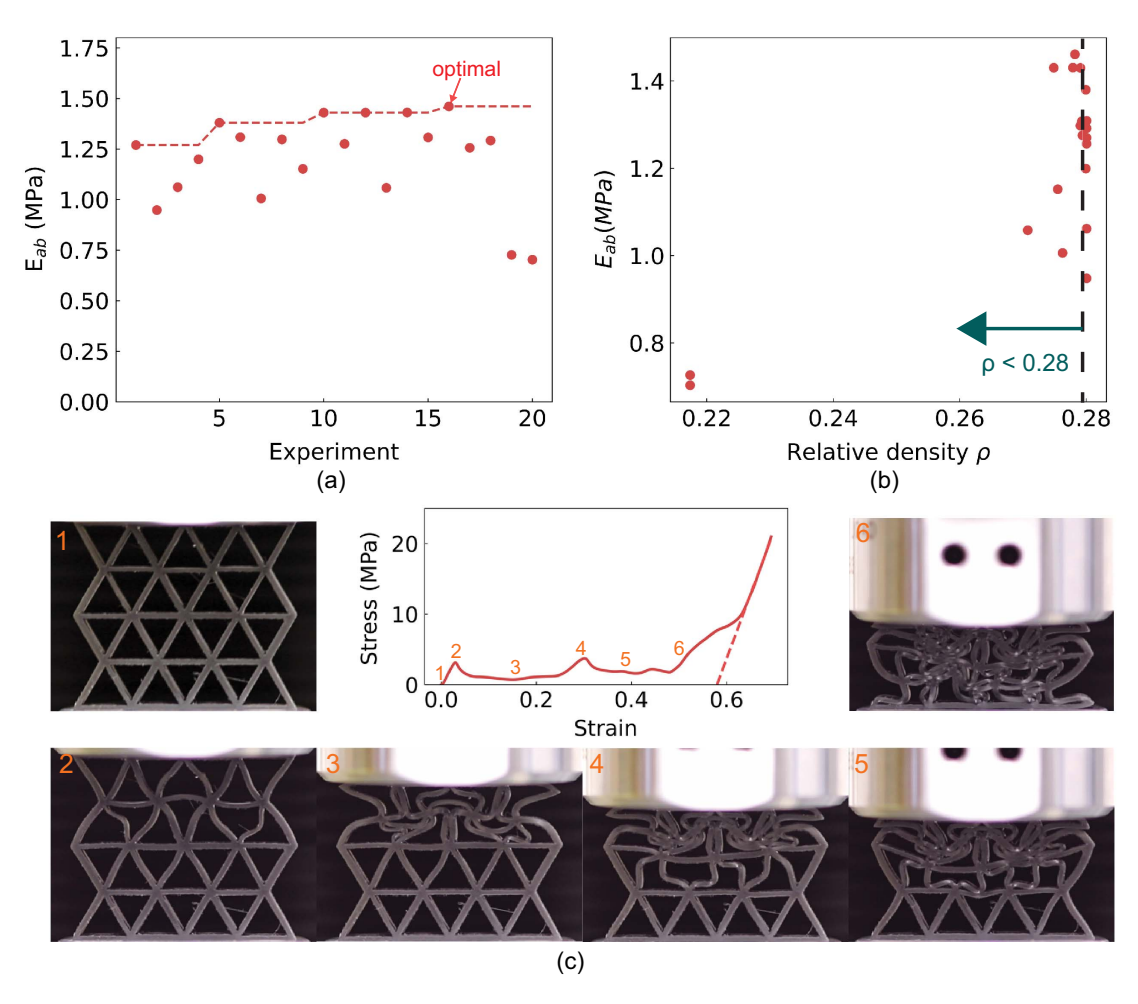


Fig. 4. Multifidelity BO with constrained relative density: (a) energy absorption of each experimental iteration with accumulated maxima; (b) energy absorption versus relative density, showing all iterations that satisfy the constraint; and (c) stress–strain behavior and optical images of the lattice at various stages of compression (indicated by the numbers) for the best-performing lattice with maximized energy absorption that satisfies the relative density constraint (Video S3).

of plateau stress. Out of 40 experiments, 17 experiments satisfied the constraint. The penalty for exceeding the constraint was applied in the acquisition function, requiring that the optimization process balances the search for optimal values with constraint satisfaction. An alternative approach would be to require a separate optimization loop to learn the constraint space separately. However, this would require additional experiments.

The sequence of deformation of the best-performing lattice is shown, along with its stress–strain response, in Fig. 5(c) (with actual measured properties given in Table 1). The stress plateau was much flatter than the stress plateau for the best-performing lattice optimized without constraints. Also, the deformation pattern was different than it was in the prior two examples. Initial buckling occurred at different nodes, leading to a V-shape pattern, rather than sequential, row-by-row buckling. This initial buckling pattern preserves the top and bottom layers while crushing the diagonal struts, ultimately resulting in a much smoother stress–strain response.

Discussion

In this work, multifidelity Bayesian optimization was found to accelerate the convergence process of optimization with 16 independent continuous variables. We were able to find optimal nonuniform triangular lattices with maximal energy absorption during compression with just 15 iterations (one experiments and 10 simulations in

each iteration, executed in parallel). This improvement was aided by the correlation between high-fidelity experiments and low-fidelity simulations, allowing more low-fidelity data to be acquired in parallel to speed up the convergence. BO with only experimental data (high-fidelity) did not show signs of convergence after 20 iterations. Because the convergence rate of Bayesian optimization was expected to deteriorate in high-dimensional input spaces, we anticipated that more than 100 iterations of high-fidelity experiments may be required [we can deduce that via our low-fidelity-only campaigns shown in Fig. S1 as well as prior work with 17D categorical parameters (Vangelatos et al. 2021)]. The use of multifidelity data sources provided enormous savings, both of material cost and of time.

Moreover, optimizing with MFBO does not require that numerical simulations capture every detail of the experiments, relaxing the need for specialized, application-specific knowledge and for laborious parameter tuning. For comparison, a previous study with one-fourth the number of continuous variables required twice the number of experiments to reach convergence with single-fidelity BO (Gongora et al. 2020). Another work with a similar number of parameters (17 categorical parameters) reached convergence after 250 iterations with single-fidelity BO, using numerical simulations (Vangelatos et al. 2021). In contrast, our BO method, incorporating multifidelity data sources, yielded optimal structures with only 15 high-fidelity experiments for a problem with 16 continuous variables. This shows the possibility that by utilizing multifidelity

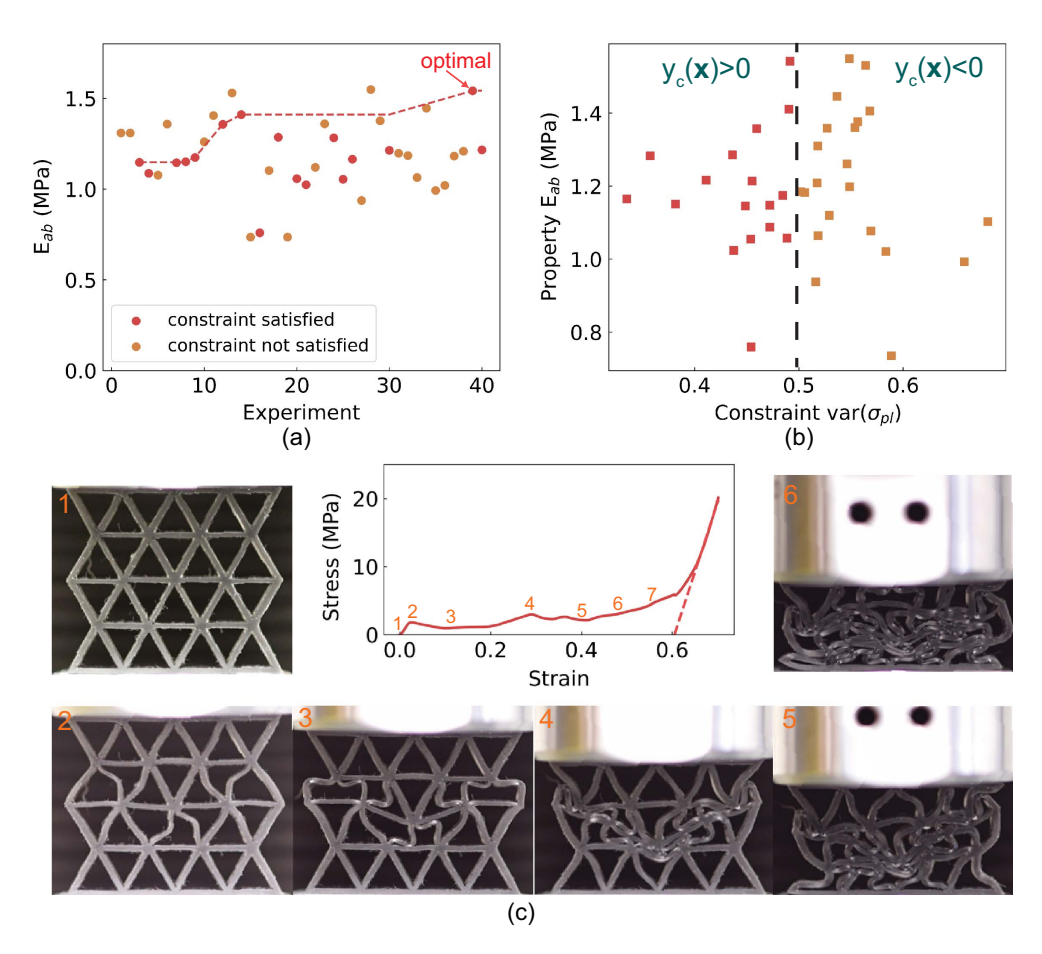


Fig. 5. Multifidelity BO with a constraint on the variance of plateau stress: (a) energy absorption of each experimental iteration, with accumulated maxima and satisfaction of the constraints; (b) energy absorption versus variance of the plateau stress, showing the distribution of iterations, indicating whether the constraint is satisfied; and (c) stress–strain relationship and optical images of the deformed lattice at various stages of compression for the lattice with maximal energy absorption that also satisfies the constraint on the variance of the plateau stress (Video S4).

sources, one can tackle problems with much larger numbers of parameters. However, one should still keep in mind that computation of conventional BO is limited to problems of relatively low dimension (fewer than 25 dimensions). This is an active area of research, with multiple recent works aimed at addressing the dimensional limitation of BO (Maddox et al. 2021; Kirschner et al. 2019; Wang et al. 2016).

Our proposed framework can be easily transferred to other systems, with limited complex experiments performed by humans combined with automated numerical simulations to accelerate the convergence process. There are further improvements that could be made to the framework, leading to overall performance of the optimization. The acquisition function can be modified to incorporate the respective costs of high- and low-fidelity data sources, similar to previous multiple simulation frameworks (Couperthwaite et al. 2020). Furthermore, a multifidelity multiobjective BO could unlock complexity while optimizing for multiple properties.

Materials and Methods

3D Printing and Materials

The materials in this work were printed with an EnvisionTEC (Detroit) desktop digital light projection resin 3D printer (Vida HD). The printer has a build volume of $96 \times 54 \times 100 \text{ mm}^3$ with XY resolution = $50 \ \mu\text{m}$ and a z step size of $50 \ \mu\text{m}$. The printer

takes grayscale images $(1,920 \times 1,080)$ as inputs which, which are projected into the resin. The material used in this work was a proprietary photopolymer named E-rigid PU black. Mechanical properties of the E-rigid PU black were measured by conducting uniaxial tensile tests at a strain rate of 0.002/s using an Instron 65SC (Norwood, Massachusetts).

Numerical Simulations

Numerical simulations of lattice compression were conducted using ABAQUS version 2020 Explicit analysis. The structures were compressed 80% in 100 s. The total simulation time was determined such that the total kinetic energy would not exceed 5% of total internal energy throughout the simulation. Contact between all surfaces was defined with zero friction and hard contact. The material was assumed to be perfectly plastic, with Young's modulus of 1,200 MPa and yield stress of 30 MPa, as measured via uniaxial tensile tests of the material.

Lattice Compression

The triangular cellular structure has a unit cell length of 10 mm and an out-of-plane thickness of 6 mm. Compression of cellular structures was conducted with an Instron 68SC using compression plates of 50 -mm diameter, at a strain rate of 0.002/s. The compression was stopped at either 60% strain or when the force exceeded the limit of 5,000 N.

Gaussian Process

The Gaussian process used in this work was implemented with radial basis function (RBF) kernel in covariance matrix and uniform Gaussian prior. For an input with dimension d, the RBF kernel can be computed as follows:

$$k(\mathbf{x}, \mathbf{x}') = \sigma^2 \exp\left(-\frac{1}{2} \sum_{i=1}^d \frac{(x_i - x_i')^2}{l_i^2}\right)$$
 (6)

where σ and $\mathbf{l} = [l_1, l_2, \dots, l_d]$ together constitute the training parameter θ . Training is done by maximizing the marginal likelihood

$$\log p(\mathbf{y}|\mathbf{x}, \theta) = -\frac{1}{2}\log |\mathbf{K} + \sigma_{\epsilon}^{2}\mathbf{I}| - \frac{1}{2}\mathbf{y}^{T}(\mathbf{K} + \sigma_{\epsilon}^{2}\mathbf{I})^{-1}\mathbf{y} - \frac{N}{2}\log 2\pi$$
(7)

where $\mathbf{K} = \mathbf{k}(\mathbf{x}, \mathbf{x}'; \theta)$ is the covariance matrix computed from all dimensions of input \mathbf{x} using the kernel definition in Eq. (6) with additional training parameter σ_{ε} . After training the Gaussian process model, a prediction in terms of mean and standard deviation can be computed on \mathbf{x}^* as follows:

$$\mu(\mathbf{x}^*) = \mathbf{k}(\mathbf{x}^*, \mathbf{x}; \theta)(\mathbf{K} + \sigma_{\epsilon}^2 \mathbf{I})^{-1} \mathbf{y}$$
 (8)

$$\sigma(\mathbf{x}^*) = \mathbf{k}(\mathbf{x}^*, \mathbf{x}^*; \theta) - \mathbf{k}(\mathbf{x}^*, \mathbf{x}; \theta)(\mathbf{K} + \sigma_{\epsilon}^2 \mathbf{I})\mathbf{k}(\mathbf{x}, \mathbf{x}^*; \theta)$$
(9)

Multifidelity Gaussian Process

We define observations in both high and low fidelity as follows:

$$\mathbf{y_H} = f_H(\mathbf{x_H}) + \epsilon_H$$

$$\mathbf{y_L} = f_L(\mathbf{x_L}) + \epsilon_L \tag{10}$$

We assumed the observations have a Gaussian distribution with independent kernels and uncertainties as follows:

$$\mathbf{y_H} \sim \mathcal{GP}(0, \mathbf{k_H}(\mathbf{x_H}, \mathbf{x'_H}), \sigma_H))$$

$$\mathbf{y_L} \sim \mathcal{GP}(0, \mathbf{k_L}(\mathbf{x_L}, \mathbf{x'_L}), \sigma_L))$$
(11)

The inputs and output are combined $\mathbf{y} = [\mathbf{y_L}; \mathbf{y_H}], \mathbf{X} = [\mathbf{x_L}; \mathbf{x_H}].$ In addition, we assumed a linear relation between the low-fidelity observations and high-fidelity observations, with the following parameters:

$$\mathbf{y_H}(\mathbf{x}) = \rho \mathbf{y_L}(\mathbf{x}) + \delta(\mathbf{x}) \tag{12}$$

For the multifidelity Gaussian process, the training parameter now includes θ_L, θ_H, ρ . To train the model, the marginal likelihood is again maximized

$$\log p(\mathbf{y}|\mathbf{x}, \theta_L, \theta_H, \rho) = -\frac{1}{2}\log |\mathbf{K}| - \frac{1}{2}\mathbf{y}^T\mathbf{K}^{-1}\mathbf{y} - \frac{N_L + N_H}{2}\log 2\pi$$
(13)

Here, the covariance matrix includes both low-fidelity and high-fidelity observations and can be constructed as follows:

$$\mathbf{K} = \begin{bmatrix} \mathbf{k}(\mathbf{x}_{\mathbf{L}}, \mathbf{x}_{\mathbf{L}}'; \theta_{L}) + \sigma_{L}^{2} \mathbf{I} & \rho \mathbf{k}_{\mathbf{L}}(\mathbf{x}_{\mathbf{L}}, \mathbf{x}_{\mathbf{H}}'; \theta_{L}) \\ \rho \mathbf{k}_{\mathbf{L}}(\mathbf{x}_{\mathbf{H}}, \mathbf{x}_{\mathbf{L}}'; \theta_{L}) & \rho^{2} \mathbf{k}_{\mathbf{L}}(\mathbf{x}_{\mathbf{H}}, \mathbf{x}_{\mathbf{H}}', \theta_{L}) + \mathbf{k}_{\mathbf{H}}(\mathbf{x}_{\mathbf{H}}, \mathbf{x}_{\mathbf{H}}'; \theta_{H}) + \sigma_{H}^{2} \mathbf{I} \end{bmatrix}$$

$$(14)$$

Predictions can be made with trained parameters in the prediction space \mathbf{x}^*

$$\mu(\mathbf{x}^*) = \mathbf{k}(\mathbf{x}^*, \mathbf{X})\mathbf{K}^{-1}\mathbf{y} \tag{15}$$

$$\sigma(\mathbf{x}^*) = \mathbf{k}(\mathbf{x}^*, \mathbf{x}^*) - \mathbf{k}(\mathbf{x}^*, \mathbf{X})\mathbf{K}^{-1}\mathbf{k}(\mathbf{X}, \mathbf{x}^*)$$
(16)

Bayesian Optimization Algorithm

The BO algorithm in this work was built using JAX library (Perdikaris 2020), enabling high-efficiency automatic differentiation accelerated with processing units. Our algorithm used both a single-fidelity Gaussian process and a multifidelity Gaussian process to provide predictions for the entire space. Next, we computed the next point of evaluation by minimizing the acquisition function. The acquisition used in this work was the lower confidence bound (LCB), which can be computed with parameter κ and prediction of the Gaussian process

$$LCB(\mathbf{x}) = \mu(\mathbf{x}) - \kappa \sigma(\mathbf{x}) \tag{17}$$

Data Availability Statement

Some or all data, models, or code that support the findings of this study are available from the corresponding author upon reasonable request.

Acknowledgments

CM and JRR gratefully acknowledge support via the University of Pennsylvania Materials Research Science and Engineering Center (MRSEC) (NSF DMR-1720530), AFOSR Grant No. FA9550-22-1-0163, and by a 3M Non-Tenured Faculty Award. PP gratefully acknowledges support via DOE Grant No. DE-SC0019116.

Supplemental Materials

Figs. S1–S3 and Videos S1–S4 are available online in the ASCE Library (www.ascelibrary.org).

References

Balachandran, P. V., B. Kowalski, A. Sehirlioglu, and T. Lookman. 2018. "Experimental search for high-temperature ferroelectric perovskites guided by two-step machine learning." *Nat. Commun.* 9 (1): 1668. https://doi.org/10.1038/s41467-018-03821-9.

Buhl, T., C. B. W. Pedersen, and O. Sigmund. 2000. "Stiffness design of geometrically nonlinear structures using topology optimization." *Struct. Multidiscip. Optim.* 19 (2): 93–104. https://doi.org/10.1007/s00158005

Burger, B., et al. 2020. "A mobile robotic chemist." *Nature* 583 (7815): 237–241. https://doi.org/10.1038/s41586-020-2442-2.

- Chen, C., Y. Zuo, W. Ye, X. Li, and S. P. Ong. 2021. "Learning properties of ordered and disordered materials from multi-fidelity data." *Nat. Comput. Sci.* 1 (1): 46–53. https://doi.org/10.1038/s43588-020-00002-x.
- Chen, E., S. Luan, and S. Gaitanaros. 2022. "On the strength of brittle foams with uniform and gradient densities." *Extreme Mech. Lett.* 51 (Feb): 101598. https://doi.org/10.1016/j.eml.2021.101598.
- Couperthwaite, R., A. Molkeri, D. Khatamsaz, A. Srivastava, D. Allaire, and R. Arròyave. 2020. "Materials design through batch bayesian optimization with multisource information fusion." *JOM* 72 (12): 4431–4443. https://doi.org/10.1007/s11837-020-04396-x.
- Da, D., Y.-C. Chan, L. Wang, and W. Chen. 2022. "Data-driven and topological design of structural metamaterials for fracture resistance." *Extreme Mech. Lett.* 50 (Jan): 101528. https://doi.org/10.1016/j.eml .2021.101528.
- Da, D., and X. Qian. 2020. "Fracture resistance design through biomimicry and topology optimization." *Extreme Mech. Lett.* 40 (Oct): 100890. https://doi.org/10.1016/j.eml.2020.100890.
- Dixon, P. G., and L. J. Gibson. 2014. "The structure and mechanics of moso bamboo material." J. R. Soc. Interface 11 (99): 20140321. https://doi. org/10.1098/rsif.2014.0321.
- Erps, T., M. Foshey, M. K. Luković, W. Shou, H. H. Goetzke, H. Dietsch, K. Stoll, B. von Vacano, and W. Matusik. 2021. "Accelerated discovery of 3d printing materials using data-driven multiobjective optimization." Sci. Adv. 7 (42): eabf7435. https://doi.org/10.1126/sciadv.abf7435.
- Frazier, P. I. 2018. "A tutorial on Bayesian optimization. "Preprint, submitted July 8, 2018. https://arxiv.org/abs/1807.02811.
- Gibson, L. J., and M. F. Ashby. 1997. "Cellular solids: Structure and properties." In *Cambridge solid state science series*. 2nd ed. Cambridge, UK: Cambridge University Press.
- Gongora, A. E., K. L. Snapp, E. Whiting, P. Riley, K. G. Reyes, E. F. Morgan, and K. A. Brown. 2021. "Using simulation to accelerate autonomous experimentation: A case study using mechanics." iScience 24 (4): 102262. https://doi.org/10.1016/j.isci.2021.102262.
- Gongora, A. E., B. Xu, W. Perry, C. Okoye, P. Riley, K. G. Reyes, E. F. Morgan, and K. A. Brown. 2020. "A bayesian experimental autonomous researcher for mechanical design." Sci. Adv. 6 (15): eaaz1708. https://doi.org/10.1126/sciadv.aaz1708.
- Gu, G. X., C.-T. Chen, and M. J. Buehler. 2018. "De novo composite design based on machine learning algorithm." Extreme Mech. Lett. 18 (10): 19–28. https://doi.org/10.1016/j.eml.2017.10.001.
- Habibi, M. K., and Y. Lu. 2014. "Crack propagation in bamboo's hierarchical cellular structure." Sci. Rep. 4 (1): 5598.
- Hanakata, P. Z., E. D. Cubuk, D. K. Campbell, and H. S. Park. 2018. "Accelerated search and design of stretchable graphene kirigami using machine learning." *Phys. Rev. Lett.* 121 (Jan): 255304. https://doi.org/10.1103/PhysRevLett.121.255304.
- Jiang, Z., and J. H. Pikul. 2021. "Centimetre-scale crack-free self-assembly for ultra-high tensile strength metallic nanolattices." *Nat. Mater.* 20 (11): 1512–1518. https://doi.org/10.1038/s41563-021-01039-7.
- Kirschner, J., M. Mutny, N. Hiller, R. Ischebeck, and A. Krause. 2019. "Adaptive and safe bayesian optimization in high dimensions via one-dimensional subspaces." In *Proc., Int. Conf., on Machine Learning*, 3429–3438. Ithaca, NY: Cornell Univ. https://arxiv.org/abs/1902.03229.
- Li, Z., et al. 2020. "Robot-accelerated perovskite investigation and discovery." Chem. Mater. 32 (13): 5650–5663. https://doi.org/10.1021/acs.chemmater.0c01153.
- Liu, C., J. Lertthanasarn, and M.-S. Pham. 2021. "The origin of the boundary strengthening in polycrystal-inspired architected materials." *Nat. Commun.* 12 (1): 4600. https://doi.org/10.1038/s41467-021 -24886-z.
- Maddox, W. J., M. Balandat, A. G. Wilson, and E. Bakshy. 2021. "Bayesian optimization with high-dimensional outputs." Adv. Neural Inf. Process. Syst. 34 (Jun): 19274–19287. https://doi.org/10.48550/arXiv.2106.12997.
- Mao, Y., Q. He, and X. Zhao. 2020. "Designing complex architectured materials with generative adversarial networks." Sci. Adv. 6 (17): eaaz4169. https://doi.org/10.1126/sciadv.aaz4169.

- Meredig, B., et al. 2018. "Can machine learning identify the next high-temperature superconductor? Examining extrapolation performance for materials discovery." *Mol. Syst. Des. Eng.* 3 (39): 819–825. https://doi.org/10.1039/C8ME00012C.
- Meza, L. R., S. Das, and J. R. Greer. 2014. "Strong, lightweight, and recoverable three-dimensional ceramic nanolattices." *Science* 345 (6202): 1322–1326. https://doi.org/10.1126/science.1255908.
- Mirkhalaf, M., A. K. Dastjerdi, and F. Barthelat. 2014. "Overcoming the brittleness of glass through bio-inspiration and micro-architecture." *Nat. Commun.* 5 (1): 1–9. https://doi.org/10.1038/ncomms4166.
- Montgomery, S. M., H. Hilborn, C. M. Hamel, X. Kuang, K. N. Long, and H. J. Qi. 2021. "The 3d printing and modeling of functionally graded kelvin foams for controlling crushing performance." *Extreme Mech. Lett.* 46 (Jan): 101323. https://doi.org/10.1016/j.eml.2021.101323.
- Perdikaris, P. 2020. "JAX-BO: A Bayesian optimization library in JAX." Accessed March 1, 2020. https://github.com/PredictiveIntelligenceLab/JAX-BO.
- Pham, M. S., C. Liu, I. Todd, and J. Lertthanasarn. 2019. "Damage-tolerant architected materials inspired by crystal microstructure." *Nature* 565 (7739): 305–311. https://doi.org/10.1038/s41586-018-0850-3.
- Portela, C. M., B. W. Edwards, D. Veysset, Y. Sun, K. A. Nelson, D. M. Kochmann, and J. R. Greer. 2021. "Supersonic impact resilience of nanoarchitected carbon." *Nat. Mater.* 20 (11): 1491–1497. https://doi.org/10.1038/s41563-021-01033-z.
- Santer, M., and S. Pellegrino. 2009. "Topological optimization of compliant adaptive wing structure." *AIAA J.* 47 (3): 523–534. https://doi.org/10.2514/1.36679.
- Santos, A. G., G. O. da Rocha, and J. B. de Andrade. 2019. "Occurrence of the potent mutagens 2-nitrobenzanthrone and 3-nitrobenzanthrone in fine airborne particles." *Sci. Rep.* 9 (1): 1. https://doi.org/10.1038/s41598-018-37186-2.
- Smith, M. L., N. Napp, and K. H. Petersen. 2021. "Imperfect comb construction reveals the architectural abilities of honeybees." *Proc. Natl. Acad. Sci. U.S.A.* 118 (31): e2103605118. https://doi.org/10.1073/pnas.2103605118.
- Snoek, J., H. Larochelle, and R. P. Adams. 2012. Practical Bayesian optimization of machine learning algorithms. https://doi.org/10.48550/arXiv.1206.2944.
- Solomou, A., G. Zhao, S. Boluki, J. K. Joy, X. Qian, I. Karaman, R. Arròyave, and D. C. Lagoudas. 2018. "Multi-objective bayesian materials discovery: Application on the discovery of precipitation strengthened niti shape memory alloys through micromechanical modeling." *Mater. Des.* 160 (14): 810–827. https://doi.org/10.1016/j.matdes.2018 .10.014.
- Song, J., Y. Wang, W. Zhou, R. Fan, B. Yu, Y. Lu, and L. Li. 2019. "Topology optimization-guided lattice composites and their mechanical characterizations." *Composites, Part B* 160 (12): 402–411. https://doi.org/10.1016/j.compositesb.2018.12.027.
- Stach, E., et al. 2021. "Autonomous experimentation systems for materials development: A community perspective." *Matter* 4 (9): 2702–2726. https://doi.org/10.1016/j.matt.2021.06.036.
- Torres, A. M., A. A. Trikanad, C. A. Aubin, F. M. Lambers, M. Luna, C. M. Rimnac, P. Zavattieri, and C. J. Hernandez. 2019. "Bone-inspired microarchitectures achieve enhanced fatigue life." *Proc. Natl. Acad. Sci. U.S.A.* 116 (49): 24457–24462. https://doi.org/10.1073/pnas.1905814116.
- Vangelatos, Z., H. M. Sheikh, P. S. Marcus, C. P. Grigoropoulos, V. Z. Lopez, G. Flamourakis, and M. Farsari. 2021. "Strength through defects: A novel bayesian approach for the optimization of architected materials." Sci. Adv. 7 (41): eabk2218. https://doi.org/10.1126/sciadv.abk2218.
- Wang, Z., F. Hutter, M. Zoghi, D. Matheson, and N. De Feitas. 2016. "Bayesian optimization in a billion dimensions via random embeddings." *J. Artif. Intell. Res.* 55 (Jun): 361–387. https://doi.org/10.1613/jair.4806.
- Xue, D., P. V. Balachandran, J. Hogden, J. Theiler, D. Xue, and T. Lookman. 2016. "Accelerated search for materials with targeted properties by adaptive design." *Nat. Commun.* 7 (1): 11241. https://doi.org/10.1038/ncomms11241.

- Yang, C., Y. Kim, S. Ryu, and G. X. Gu. 2020. "Prediction of composite microstructure stress-strain curves using convolutional neural networks." *Mater. Des.* 189 (45): 108509. https://doi.org/10.1016/j.matdes.2020 .108509.
- Yin, Z., F. Hannard, and F. Barthelat. 2019. "Impact-resistant nacre-like transparent materials." *Science* 364 (6447): 1260–1263. https://doi.org/10.1126/science.aaw8988.
- Yu, C.-H., Z. Qin, and M. J. Buehler. 2019. "Artificial intelligence design algorithm for nanocomposites optimized for shear crack resistance." *Nano Futures* 3 (3): 035001. https://doi.org/10.1088/2399-1984/ab36f0.
- Yuan, R., Z. Liu, P. V. Balachandran, D. Xue, Y. Zhou, X. Ding, J. Sun, D. Xue, and T. Lookman. 2018. "Accelerated discovery of large electrostrains in batio3-based piezoelectrics using active learning." Adv. Mater. 30 (7): 1702884. https://doi.org/10.1002/adma.201702884.
- Zheng, X., et al. 2014. "Ultralight, ultrastiff mechanical metamaterials." *Science* 344 (6190): 1373–1377. https://doi.org/10.1126/science .1252291.
- Zhong, M., et al. 2020. "Accelerated discovery of co2 electrocatalysts using active machine learning." *Nature* 581 (7807): 178–183. https://doi.org/10.1038/s41586-020-2242-8.